Journal of Science and Transport Technology
Journal homepage: https://jstt.vn/index.php/en

# Elastic and failure properties of 2D primitive TPMS lattices with varying shape factor

Dinh-Thao-Anh Truong, Minh-Cuong Le, Hoang-Quan Nguyen, Bao-Viet Tran, Anh-Tuan Tong*
University of Transport and Communications, No.3 Cau Giay Street, Lang Ward, Ha Noi, Viet Nam

**Article info**
**Type of article:**
Original research paper

**DOI:**
https://doi.org/10.58845/jstt.utt.2026.en.6.4.48-61

***Corresponding author:**
Email address:
tatuan@utc.edu.vn

**Received:** 21/11/2025
**Received in Revised Form:** 27/04/2026
**Accepted:** 30/05/2026

**Abstract:** Architected materials based on Triply Periodic Minimal Surfaces (TPMS) have demonstrated outstanding mechanical performance; however, their two-dimensional (2D) counterparts remain insufficiently explored. This study presents a comprehensive numerical investigation of the elastic response and failure behavior of 2D Primitive TPMS lattice structures, with particular emphasis on the role of geometric parameters $C_1$ and $C_2$. A phase-field damage framework is employed to capture the full mechanical evolution, from initial elastic deformation to crack initiation and subsequent propagation leading to ultimate failure. The results reveal that mechanical performance is governed not only by relative density but also critically by geometric configuration. In particular, structures with nearly identical relative densities can exhibit strength variations of up to five times, underscoring the dominant influence of shape parameters. In addition, certain configurations display pronounced auxetic behavior, with a minimum Poisson's ratio of −0.12 observed for $C_1 = 1.2$ and $C_2 = 0.8$. Failure consistently initiates at the specimen center, where stress concentration is most severe. Overall, this study provides both a high-quality numerical dataset and fundamental insights into the geometry–mechanical performance relationship of 2D TPMS lattices. The findings establish a foundation for the rational design and optimization of TPMS-based architected materials in advanced engineering applications.

**Keywords:** Primitive; damage behavior; phase field method; 3D printing; auxetic.

## 1. Introduction

The relentless pursuit of materials with superior performance and multi-functionality has long been a central theme in materials science and engineering. Traditionally, this pursuit was constrained by the inherent limitations of conventional manufacturing processes, such as casting, forging, and machining, which excel at creating bulk forms but struggle with intricate internal architectures. The emergence and maturation of Additive Manufacturing (AM) technologies, however, have catalyzed a fundamental revolution. By constructing components in a layer-by-layer fashion directly from digital models, AM eliminates many traditional design-for-manufacturing constraints, unlocking unprecedented geometric freedom. This has given rise to the field of architected materials or metamaterials, where the material's properties are determined not only by its chemical composition but more significantly by its precisely engineered internal structure. Through the deliberate design of

cellular solids and lattice structures, it is now possible to develop materials with highly tailored and often counter-intuitive properties, such as exceptional stiffness-to-weight ratios, negative Poisson's ratios (auxetics), and programmable energy absorption profiles, creating transformative opportunities in high-value sectors including aerospace, biomedical engineering, and robotics [1].

Within the vast design space of architected materials, lattice structures based on TPMS have distinguished themselves as a particularly compelling class [2]. Originating from differential geometry, TPMS are formally defined as surfaces that are periodic in three orthogonal directions and possess a mean curvature of zero at every point. This inherent mathematical property of area minimization results in structures that are not only lightweight but also mechanically efficient. A critical advantage of TPMS topologies – such as the Gyroid, Diamond, and Primitive surfaces – over conventional strut-based lattices arises from their continuous, smoothly curved surface geometry. Strut-based lattices inevitably contain sharp nodes or junctions where stress concentrations accumulate, acting as preferential sites for crack initiation and ultimately leading to premature failure. In stark contrast, TPMS structures are composed of continuous, smooth, and non-self-intersecting surfaces [3]. This "node-free" nature promotes a more homogeneous distribution of stress under mechasnical loading, thereby enhancing load-bearing capacity, damage tolerance, and fatigue life. Furthermore, their highly interconnected, non-tortuous pore networks facilitate efficient fluid flow and mass transfer, rendering them ideal candidates for multi-functional applications such as compact heat exchangers, catalytic substrates, and scaffolds for bone tissue regeneration [4].

While the scientific literature is replete with investigations into the mechanical, thermal, and fluidic properties of three-dimensional (3D) TPMS lattices, a discernible research gap exists in the fundamental understanding of their two-dimensional (2D) counterparts [5]. This paper specifically directs its focus towards porous structures derived from the 2D Primitive topology. These 2D configurations, while geometrically simpler, are far from trivial; they represent a fundamental building block for understanding more complex hierarchical and graded designs. Moreover, they offer significant practical advantages, including drastically reduced computational expense for numerical simulations, accelerated manufacturing speeds, and direct applicability to planar or plate-like components where in-plane mechanical performance is paramount. Applications such as advanced filtration membranes, lightweight structural cores for sandwich panels, and electrodes in next-generation batteries could directly benefit from the optimized design of these 2D structures.

A central challenge in the design of any porous material is to establish a clear and predictive relationship between its geometric parameters and its effective mechanical properties. For these 2D Primitive structures, key parameters such as porosity (and its complement, relative density) and the geometric shape factor are decisive in governing the overall response. However, a comprehensive framework that quantitatively links these design inputs to both the elastic behavior and the ultimate failure mechanisms is not yet fully established. The primary objective of this research is, therefore, to conduct a systematic investigation into the influence of porosity on the full spectrum of mechanical performance, from linear elasticity to catastrophic failure.

To address this multifaceted problem, this study employs a robust, multi-faceted computational methodology. The elastic characterization is performed using a simplified yet accurate computational model, allowing for rapid parametric analysis across a wide range of

porosities. To venture beyond the elastic limit and capture the intricate physics of material failure, we implement a phase-field damage model. This powerful continuum mechanics approach, rooted in the principles of variational fracture mechanics, is exceptionally adept at predicting complex fracture phenomena [6], [7], [8], [9]. Unlike discrete fracture methods, the phase-field model can naturally simulate crack initiation at arbitrary locations, propagation along complex paths, and even crack branching and merging without requiring ad-hoc criteria or computationally intensive remeshing procedures. The phase-field method is a powerful tool for investigating the failure mechanisms of various materials. However, most existing studies focus on tensile-dominated failure, where cracks are assumed to be driven solely by traction [10]. In this study, we aim to investigate the behavior of 2D TPMS structures under compressive loading. To achieve this objective, the multiphase-field model proposed by Lenarda et al. [11] is adopted. In this framework, two phase-field variables are introduced: $\mathrm{d}_1$ represents tensile cracking, while $\mathrm{d}_2$ accounts for compressive crushing.

By leveraging this advanced modeling technique, we aim to uncover the fundamental failure modes of $2\mathrm{D}$ Primitive structures. The insights gained will not only contribute to the fundamental science of architected materials but will also culminate in a validated design framework to guide the engineering of these novel materials for demanding, real-world applications.

## 2. Geometry configuration of $2\mathrm{D}$ primitive structure

### 2.1. Overview of Schwarz Primitive Geometry

TPMS are mathematically elegant constructs that have found profound relevance in materials design due to their unique geometric and physical properties. Among the earliest systematic studies of these surfaces were those by Hermann Amandus Schwarz in the 19th century, who classified several families of periodic minimal surfaces—including the Primitive (P), Diamond (D), and Gyroid (G) topologies. Each of these surfaces is defined implicitly as the zero level set of a scalar function $\mathrm{F}(\mathrm{x},\mathrm{y},\mathrm{z})$, which satisfies the minimal surface condition of vanishing mean curvature. The Primitive surface (P-surface), in particular, is one of the simplest yet most fundamental TPMS geometries. Its implicit equation is given by:

$$\mathrm{F}(\mathrm{x},\mathrm{y},\mathrm{z}) = \cos(\mathrm{x}) + \cos(\mathrm{y}) + \cos(\mathrm{z}) - \mathrm{C} = 0 \quad (1)$$

where $\mathrm{x},\mathrm{y},\mathrm{z}$ are Cartesian coordinates, and $\mathrm{C}$ is a tunable parameter that directly influences the morphology and porosity of the surface. For the classical case with $\mathrm{C} = 0$, the resulting surface divides space into two interpenetrating but non-overlapping labyrinths of equal volume.

While TPMS are inherently $3\mathrm{D}$, their $2\mathrm{D}$ counterparts can be constructed by considering cross-sectional slices or planar reductions of the implicit equations. In the case of the P-surface, a $2\mathrm{D}$ representation can be expressed as:

$$\mathrm{F}(\mathrm{x},\mathrm{y}) = \cos(\mathrm{x}) + \cos(\mathrm{y}) + 1 - \mathrm{C} = 0 \quad (2)$$

which yields a periodic arrangement of sinusoidal-like curves forming continuous, smooth, and interconnected networks. These $2\mathrm{D}$ Primitive structures preserve the essential topological features of the full P-surface but reduce the dimensional complexity, making them an ideal testbed for fundamental investigations. Factor 1 in Eq. (2) corresponds to the surface $\mathrm{z} = 0$. Applications of $2\mathrm{D}$ Primitive structures span a wide range of domains. In engineering design, they can be employed as lightweight cores for sandwich panels, where in-plane stiffness and energy absorption are key performance metrics. In fluidic systems, their continuous channels promote efficient transport of mass and heat, making them suitable for filtration membranes and microfluidic devices. In electrochemical systems, the ordered pore architecture offers potential advantages in battery electrodes and catalytic layers, where high surface-to-volume ratios and controlled transport pathways are essential. Thus, the $2\mathrm{D}$ Primitive

structure represents not only a simplified mathematical abstraction but also a practically valuable material architecture.

### 2.2. Influence of the Geometric Parameter C

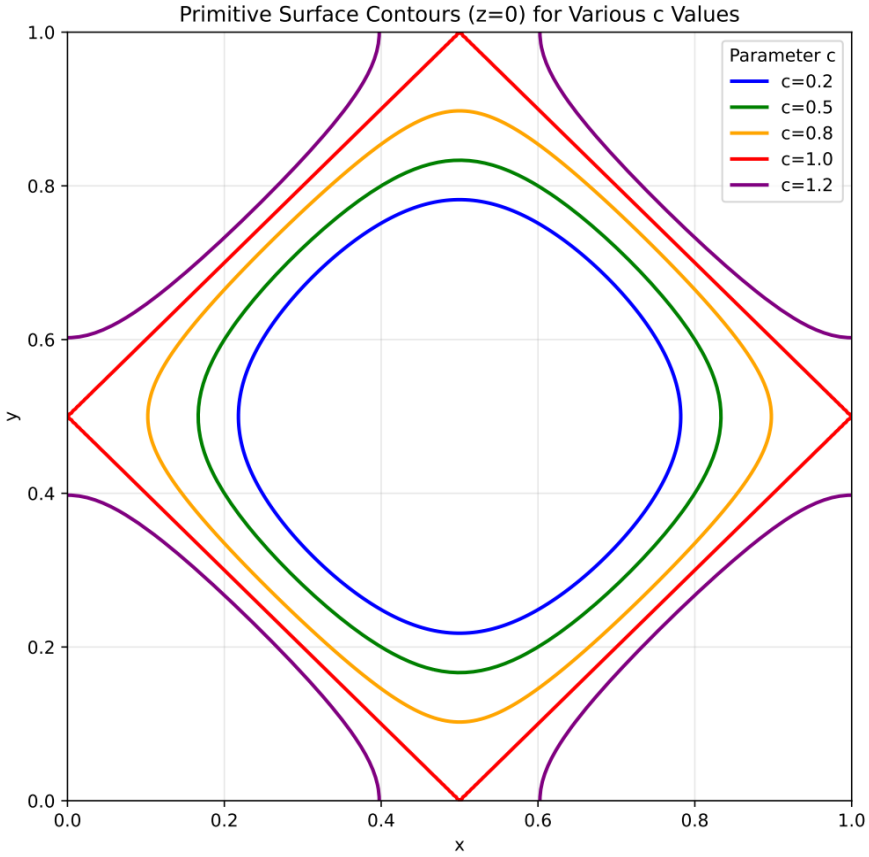


**Fig. 1**. Primitive surface geometries as a function of the shape factor C

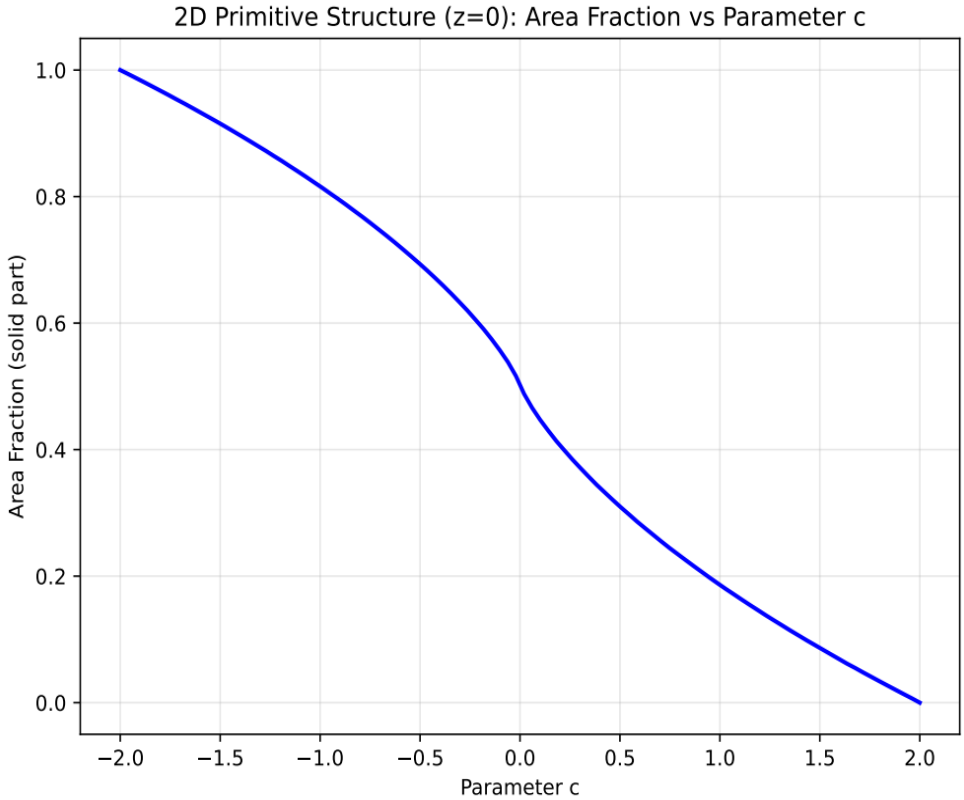


**Fig. 2.** Relationship between relative density and shape factor C

The scalar parameter $C$ in the P-surface equation plays a decisive role in governing the geometry, porosity, and mechanical behavior of the resulting structure. By systematically varying $C$, one can control the size and connectivity of the pores. Figs. 1 and 2 illustrate the influence of the parameter $C$ on the primitive surface geometry and the corresponding relative density, respectively. Three broad regimes may be identified:

Low values of $C$ (close to $0$): The structure exhibits wide, open pores with thin solid ligaments. This configuration corresponds to high porosity and low relative density, which benefits lightweight design and enhanced permeability. However, mechanical strength and stiffness are substantially reduced due to the diminished load-bearing area.

Intermediate values of $C$: The pore size and ligament thickness achieve a balanced configuration. This regime often represents an optimal trade-off between structural efficiency and permeability. From a mechanical standpoint, the stress distribution is more uniform, and failure mechanisms are delayed compared to the low-$C$ regime.

High values of $C$: As $C$ approaches its upper bound, the solid regions become dominant, and the pores shrink or even vanish. This results in low porosity and high relative density, leading to improved stiffness and strength but at the expense of reduced permeability and functionality for transport-related applications. The sensitivity of structural performance to $C$ is particularly relevant for design optimization. For example, tailoring $C$ allows the development of functionally graded structures, where porosity varies spatially to satisfy competing requirements such as mechanical load-bearing in one region and fluid transport in another. Furthermore, in numerical simulations, the variation of $C$ provides a systematic pathway to explore the correlation between geometry and effective material properties such as elastic modulus, fracture strength, and energy absorption capacity.

## 3. Numerical investigation on some mechanical properties

### 3.1. Basics of the phase field method

This section briefly summarizes the fundamental concepts of the phase-field method. The quasi-static phase-field formulation for brittle fracture proposed by Bourdin et al. [12], [13], together with the thermodynamically consistent framework developed by Miehe et al. [10], [14], constitute the pioneering models that laid the theoretical foundation of this approach. In the phase-field framework, a sharp crack is regularized and represented by a scalar damage variable $d(\mathbf{x}) \in [0,1]$, where $d = 0$ denotes the intact (undamaged) state of the material, while $d = 1$ corresponds to the fully fractured state. This formulation enables the simulation of complex crack phenomena, such as crack initiation, curvilinear crack propagation, crack branching, and crack coalescence, using a fixed finite-element mesh without the need for explicit crack tracking.

It is worth noting that, within this classical formulation, damage evolution is assumed to be driven solely by tensile loading, whereas fracture mechanisms induced by compressive stress states are neglected. Consequently, the standard phase-field method is particularly suitable for problems dominated by tensile cracking. This limitation is addressed by the multi-phase-field approach proposed by Lenarda et al., in which two scalar phase-field variables, $d_1$ and $d_2$, are introduced to represent damage induced by tensile fracture and compressive crushing, respectively.

Let us consider an arbitrary body $\Omega \in \mathbb{R}^D$, with $D$ denote the spatial dimension $(D = 1,2,3)$ and $\partial\Omega$ represents its boundary, see Fig. 3. The body contain a crack set $\Gamma = \Gamma_f \cup \Gamma_c$, where $\Gamma_f$ corresponds to fractures induced by a tensile stress state while $\Gamma_f$ represents the crushing damage caused by a compressive stress state. The total energy of a cracked body consists of the

elastic energy, the fracture energy in tension, and the crushing energy in compression:

$$E = \int_{\Omega/\Gamma} \psi(\varepsilon) d\Omega + \int_{\Gamma_f} g_f \, dS + \int_{\Gamma_c} g_c \, dS \quad (3)$$

Where $\psi$ is the elastic energy density, $\varepsilon = \frac{1}{2}(\nabla \mathbf{u} + \nabla \mathbf{u}^T)$, $g_f$, $g_c$ are the fracture energy in tension and the crushing energy in compression, respectively. In the regularized frame work, by introducing the crack density function for tensile fracture and compressive crushing, the fracture energy and the crushing energy can be approximated as follow:

$$\int_{\Gamma_f} g_f \, dS \simeq \int_{\Omega} g_f \gamma_{d_1}(d_1, \nabla d_1) d\Omega \quad (4)$$

$$\int_{\Gamma_c} g_c \, dS \simeq \int_{\Omega} g_c \gamma_{d_2}(d_2, \nabla d_2) d\Omega \quad (5)$$

Where the crack density function can be expressed as:

$$\gamma_{d_1}(d_1, \nabla d_1) = \frac{1}{2\ell_1} {d_1}^2 + \frac{\ell_1}{2} \nabla d_1 \cdot \nabla d_1 \quad (6)$$

$$\gamma_{d_2}(d_2, \nabla d_2) = \frac{1}{2\ell_2} {d_2}^2 + \frac{\ell_2}{2} \nabla d_2 \cdot \nabla d_2 \quad (7)$$

Where $\ell_1, \ell_2$ represent the crack width associated with the tensile crack and compressive crushing, respectively.

To account for the reduction in material stiffness caused by tensile fracture and compressive crushing, the phase field $d_1$ and $d_2$ are incorporated in to the elastic energy density using the following expression:

$$\psi(\boldsymbol{\varepsilon}, d_1, d_2) = ((1-d_1)^2 + \xi)\psi^+(\boldsymbol{\varepsilon}) + ((1-d_2)^2 + \xi)\psi^-(\boldsymbol{\varepsilon}) \quad (8)$$

Where $\xi$ a small positive parameter introduced to prevent numerical instability in the fully broken stateand the positive and negative part of the elastic energy density are define as:

$$\psi^{\pm}(\boldsymbol{\varepsilon}) = \frac{\lambda}{2}[\langle \mathrm{Tr}(\boldsymbol{\varepsilon}) \rangle_{\pm}]^2 + \mu \mathrm{Tr}\{(\boldsymbol{\varepsilon}^{\pm})^2\} \quad (9)$$

in which the elastic strain $\boldsymbol{\varepsilon}$ is decomposed into its positive and negative contributions as follows:

$$\boldsymbol{\varepsilon} = \boldsymbol{\varepsilon}^+ + \boldsymbol{\varepsilon}^- \quad (10)$$

$$\boldsymbol{\varepsilon}^+ = \sum_{i=1}^{D} \langle \boldsymbol{\varepsilon}^i \rangle_+ \mathbf{n}^i \otimes \mathbf{n}^i$$
$$\boldsymbol{\varepsilon}^- = \sum_{i=1}^{D} \langle \boldsymbol{\varepsilon}^i \rangle_- \mathbf{n}^i \otimes \mathbf{n}^i \quad (11)$$

Where $\varepsilon^i$ and $\mathbf{n}^i$ are the eigenvalues and eigenvector of $\boldsymbol{\varepsilon}$, satisfying $\boldsymbol{\varepsilon}\mathbf{n}^i = \varepsilon^i \mathbf{n}^i$, where the Macaulay bracket operator is defined for every scalar $x$ as $\langle x \rangle_{\pm} = (x \pm |x|)/2$. Consequently, the total energy in Eq. (3) in the regularized framework can be written as:

Eq. (12)

It is important to emphasize that in the limit $g_c \gg g_f$, this multiphase field model converge to the classic model proposed by Miehe et al. [10], [14]

$$E = \int_{\Omega} \Big( ((1-d_1)^2 + \xi)\psi^+(\varepsilon) + ((1-d_2)^2 + \xi)\psi^-(\varepsilon) + g_f \left( \frac{1}{2\ell_1} {d_1}^2 + \frac{\ell_1}{2} \nabla d_1 \cdot \nabla d_1 \right) + g_c \left( \frac{1}{2\ell_2} {d_2}^2 + \frac{\ell_2}{2} \nabla d_2 \cdot \nabla d_2 \right) \Big) d\Omega \quad (12)$$

Applying the principle of maximum dissipation and energy minimization to Eq. 12, the strong form of the tensile phase field $d_1$ and the compressive phase field $d_2$ the displacement problems can be written respectively as:

The tensile phase field:

$$\begin{cases} 2P_1(1-d_1)\mathcal{H}_f - \frac{g_c}{\ell_1}\left(d_1 - {\ell_1}^2 \Delta d_1\right) = 0 \text{ in } \Omega \\ d_1(\mathbf{x}) = 1 \text{ on } \Gamma_f \\ \nabla d_1(\mathbf{x}) \cdot \mathbf{n} = 0 \text{ on } \partial\Omega \end{cases} \quad (13)$$

The compressive phase field:

$$\begin{cases} 2P_2(1-d_2)\mathcal{H}_c - \frac{g_c}{\ell_2}\left(d_2 - {\ell_2}^2 \Delta d_2\right) = 0 \text{ in } \Omega \\ d_2(\mathbf{x}) = 1 \text{ on } \Gamma_c \\ \nabla d_2(\mathbf{x}) \cdot \mathbf{n} = 0 \text{ on } \partial\Omega \end{cases} \quad (14)$$

where

$$P_1 = \begin{cases} 1 \text{ when } \mathrm{Tr}(\sigma) > 1 \\ 0 \end{cases}$$
$$P_2 = 1 - P_1 \quad (15)$$

The history strain energy density funtion is

introduced to describe a dependence on history and possible loading-unloading:

$$\mathcal{H}_f(\mathbf{x},t) = \max_{\tau\in[0,t]}\{(g(d_1) = (1-d_1)^2)\psi^+(\mathbf{x},t)\}$$
$$\mathcal{H}_c(\mathbf{x},t) = \max_{\tau\in[0,t]}\{(g(d_2) = (1-d_2)^2)\psi^-(\mathbf{x},t)\} \quad (16)$$

The displacement field:

$$\begin{cases} \nabla\cdot\sigma(u,d_1,d_2) = \mathbf{f} \text{ on } \Omega \\ \mathbf{u}(\mathbf{x}) = \bar{u} \text{ in } \partial\Omega_u \\ \sigma\cdot\mathbf{n} = \bar{\mathbf{F}} \text{ on } \partial\Omega_F \end{cases} \quad (17)$$

The Cauchy stress $\boldsymbol{\sigma}$ in equation (17) is defined as:

$$\boldsymbol{\sigma} = ((1-d_1)^2+\xi)\{\lambda\langle Tr\varepsilon\rangle_+\mathbf{1}+2\mu\varepsilon^+\} + ((1-d_2)^2+\xi)\{\lambda\langle Tr\varepsilon\rangle_-\mathbf{1}+2\mu\varepsilon^-\} \quad (18)$$

At each time step (load increment), Eqs. (13), (14), and (17) are solved sequentially using a standard finite element procedure within a staggered framework.

### 3.2. Numerical validation

Prior to applying the proposed multi-phase field formulation to investigate the mechanical response of two-dimensional primitive structures, a series of numerical benchmark tests is carried out to systematically assess the effect of the crushing-to-fracture energy ratio. A square domain with dimensions of 10x10 $mm^2$ is considered, comprising a two – phase material system (see Fig. 4). The domain includes a circular inclusion of radius $R = 1\ mm$ embedded in a homogeneous matrix. Both phases are assumed to exhibit linear elastic behavior. The elastic modulus and Poisson's ratio of the inclusion are $E_i = 60\ GPa, \nu_i = 0.3$, respectively, while those of matrix are $E_m = 22\ GPa, \nu_m = 0.21$. These two phases are assumed to be an elastic behavior. The fracture enery of matrix and inclusion are 1x10$^{-6}$kN/mm and 1x10$^{-4}$ kN/mm, respectively. Five crushing-to-fracture energy ratio are considered: 50; 100; 400; 1000; 2000. The characteristic length parameters governing tensile cracking and compressive crushing are assumed to be equal, with, $\ell_1 = \ell_2 = 0.2\ mm$. The constant strain triangle element is employed for all simulation in this study. The element size $h$ is set to 0.1 which satisfies the condition $h \le \ell_1/2$ and $h \le \ell_2/2$, ensuring mesh independent of the solution [10], [15]. The total number of elements is 24304.

Plane strain is assumed. The bottom edge of the domain is fully constrained in the $y$-direction, while the horizontal displacement of a single node located at the left edge is fixed in the $x$-direction to prevent rigid body motion. A monotonic compressive displacement $\bar{u} = -5x10^{-4}mm$ is imposed on the top edge of the domain.

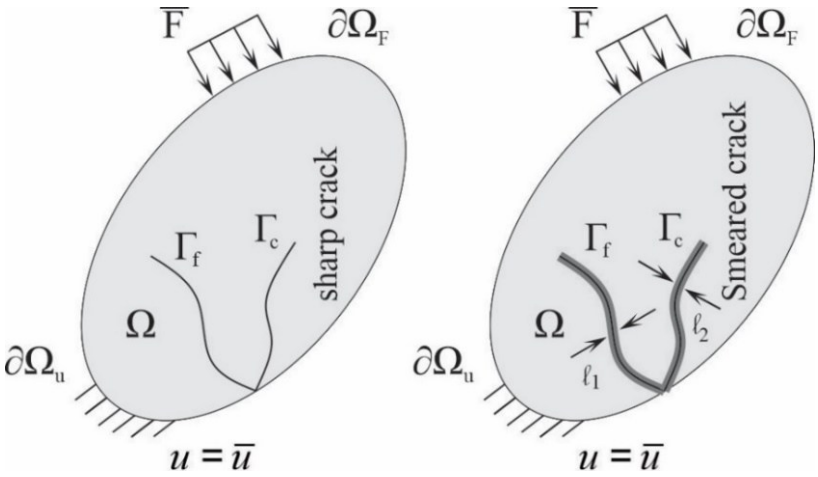


(a) Sharp crack model (b) Regularized representation through phase field

**Fig. 3.** Regularized representation of a crack

The effect of the crushing-to-fracture energy ratio on the stress–displacement response is illustrated in Fig. 5. Two noteworthy observations can be drawn from these curves. First, variations in

the crushing-to-fracture energy ratio have a negligible influence on the elastic response of the specimen. Second, within the framework of Miehe's model—where damage evolution is assumed to be governed exclusively by tensile-driven damage—the stress increases monotonically under compressive loading. This behavior implies that the specimen can sustain continuously increasing compressive loads without undergoing compressive crushing, as damage is not activated under compression. Consequently, although tensile-driven damage may still develop, the compressive response does not exhibit any stiffness or strength degradation, leading to an unrealistic representation of the mechanical behavior of real quasi-brittle materials.

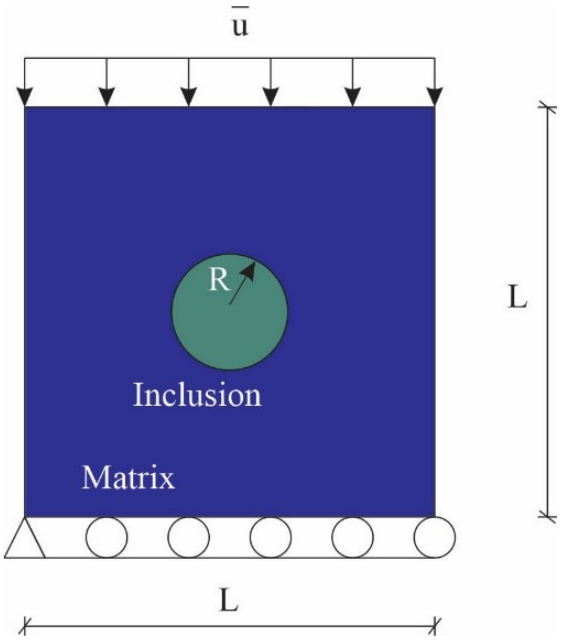


**Fig. 4.** Dimension and boundary condition of compressive test

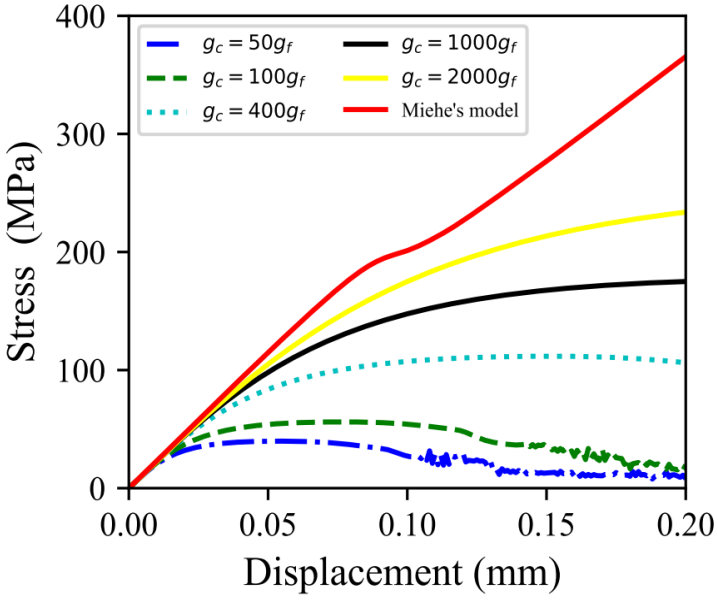


**Fig. 5.** The effect of the crushing-to-fracture energy ratio

In contrast, when the multi-phase field formulation is employed, both tensile-driven damage and compressive crushing are explicitly accounted for. As a result, a distinct softening stage emerges after the attainment of the peak stress, reflecting the progressive development of compressive crushing. Moreover, increasing the crushing-to-fracture energy ratio leads to a higher

peak stress, indicating enhanced resistance against compressive crushing. As the crushing-to-fracture energy ratio becomes sufficiently large, the contribution of compressive crushing diminishes, and the response predicted by the multi-phase field model gradually converges toward that of Miehe's model, in which tensile-driven damage dominates the overall material degradation. The responses obtained from the multi-phase field model for different crushing-to-fracture energy ratios are presented in Fig. 6. It can be observed that the predicted behavior of the multi-phase field model is highly sensitive to variations in the crushing-to-fracture energy ratio, indicating a strong influence of this parameter on the material response. Therefore, an appropriate choice of the crushing-to fracture energy ratio enables the model to provide a realistic prediction of the material response [16].

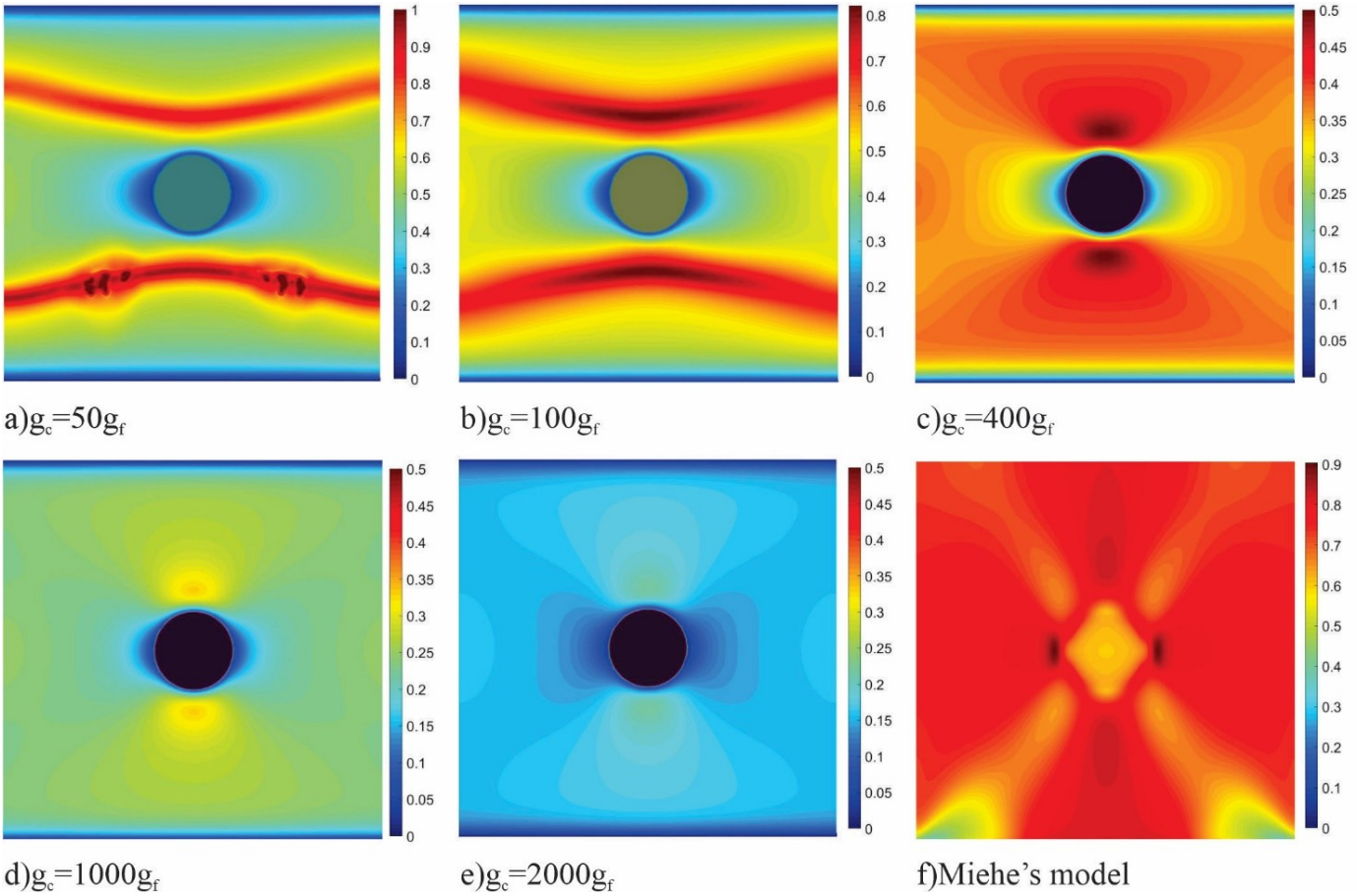


**Fig. 6.** The multi phase field with different crushing to fracture energy ratio

**Fig. 7.** Illustration of primitive sample fabricated with PLA material

**Table 1**. Mechanical properties of PLA used in the numerical study

| Property | Symbol | Value (typical) | Unit |
|---|---|---|---|
| Density | $\rho$ | $1.24$ | $\mathrm{g/cm^3}$ |
| Young's modulus | $\mathrm{E}$ | $3.5$ | $\mathrm{GPa}$ |
| Poisson's ratio | $\nu$ | $0.36$ | – |
| Tensile strength | $\sigma_t$ | $50$ | $\mathrm{MPa}$ |
| Compressive strength | $\sigma_c$ | $70$ | $\mathrm{MPa}$ |

## 4. Elastic and failure properties of 2D primitive TPMS lattices

### 4.1. Elastic and damage properties

To investigate the influence of geometric configuration on the elastic and damage behavior of the material, we conducted a numerical case study with specific parameters. The material considered was Poly Lactic Acid (PLA) plastic, commonly used for $3\mathrm{D}$-printed structures. Fig. 7 illustrates an example of TPMS geometries fabricated by the research group using PLA. The mechanical properties of the PLA employed in this study are summarized in Table 1.

Regarding the material structure, we focused on porous systems defined by two primitive surfaces characterized by the parameters $\mathrm{C}_1$ and $\mathrm{C}_2$. In this study, $\mathrm{C}_1$ varied from $1.2$ to $1.4$, while $\mathrm{C}_2$ ranged from $1.0$ to $0.6$. In this study, the parameters $\mathrm{C}_1$ and $\mathrm{C}_2$ represent two values of the constant c that define the inner and outer surfaces of the $2\mathrm{D}$ Primitive (P-type) TPMS lattice (see Fig. 1). Specifically, $\mathrm{C}_1 > \mathrm{C}_2$, where $\mathrm{C}_1$ corresponds to the outer boundary surface and $\mathrm{C}_2$ corresponds to the inner boundary surface. Fig. 8 illustrate the geometry and boundary condition of 2D TPMS. This domain is discretized by constant strain triangle, with a total of 69164 elements. The characteristic length parameters are chosen consistent with the previous validation case, ie, $\ell_1 = \ell_2 = 0.2\ \mathrm{mm}$. The tensile fracture is chosen as: $\mathrm{g_f} = \dfrac{256\ell_1(\sigma_t)^2}{27\mathrm{E}} = 0{,}0013\ \mathrm{kN/mm}$, the compressive fracture is chosen as $\mathrm{g_c} = \mathrm{g_f}\left(\dfrac{\sigma_c}{\sigma_t}\right)^2 = 0{,}00265\ \mathrm{kN/mm}$.

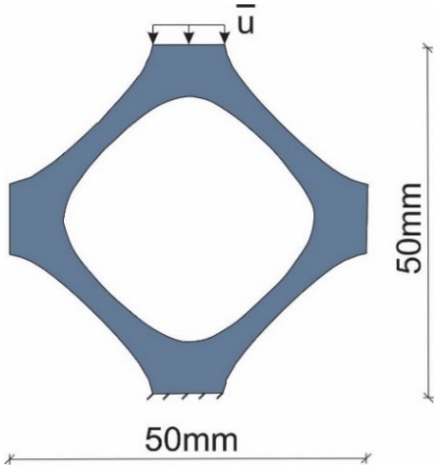


**Fig. 8.** Dimension and boundary condition of 2D TPMS lattice

Together, these two parameters determine the thickness and spatial domain of the lattice structure. The resulting geometric forms, failure locations, and stress–displacement responses are shown in Fig. 9 and Fig.10.

The results indicate a strong dependence on the density of the structure. For the case where $\mathrm{C}_1$ was fixed at $1.2$, the density decreased from $25\%$ ($\mathrm{C}_2 = 0.6$) to $19\%$ ($\mathrm{C}_2 = 0.8$) and $10\%$ ($\mathrm{C}_2 = 1.0$). Correspondingly, the critical stress dropped by a factor of approximately 3–5 at each step. Failure was initiated at the center of the specimen and subsequently propagated to the four side edges, as shown in the figures.

When $\mathrm{C}_2$ was fixed at $0.99$ and $\mathrm{C}_1$ increased, the variation in mechanical response was less pronounced compared to the change in density. Specifically, $\mathrm{C}_1 = 1.3$ corresponded to a density of $14\%$, while $\mathrm{C}_1 = 1.4$ corresponded to $17\%$. In this scenario, the plastic stage of the structural response was also more clearly observed.

In addition to density, the shape parameters

themselves play a crucial role. For example, when comparing the cases of $C_1 = 1.2$, $C_2 = 0.8$ and $C_1 = 1.4$, $C_2 = 1.0$, the densities were nearly identical; however, the strength of the former was about five times higher. The weakest point, located at the specimen's center, was found to govern the onset of damage and the overall failure process.

### 4.2. Auxetic properties

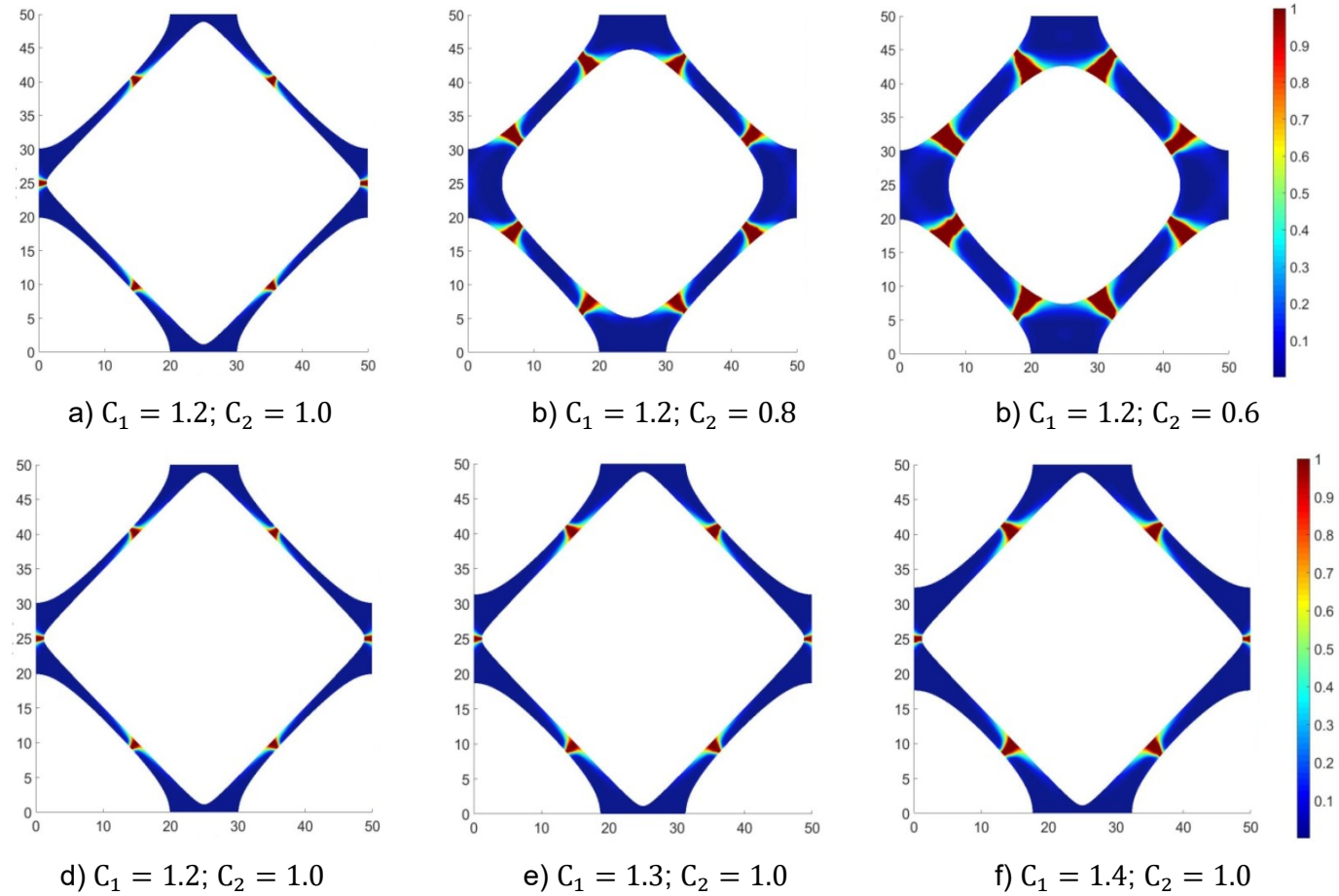


**Fig. 9.** Damage evolution of the specimen under compression

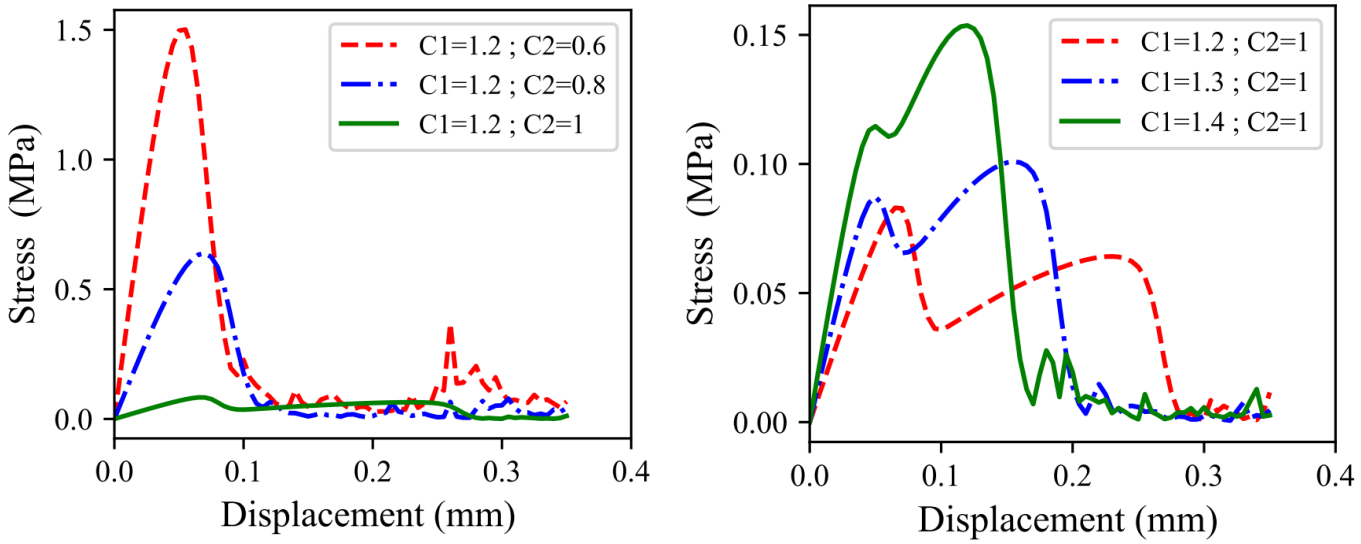


**Fig. 10.** Stress–displacement relationships for different geometric cases

An important characteristic of the proposed primitive structure is its potential to exhibit auxetic properties, a feature investigated here through numerical simulation. This study examined the

structure's capacity to generate a negative Poisson's ratio by simulating the lateral displacement of its edge under incremental axial loading, governed by geometric parameters $C_1$ and $C_2$. Our simulations revealed two distinct mechanical behaviors.

Using the aforementioned computational examples, we simulated the lateral displacement of the structure's left edge under several incremental axial displacement steps: $0.05\ \text{mm}$, $0.1\ \text{mm}$, $0.15\ \text{mm}$, and $0.2\ \text{mm}$. The results presented in Fig. 11 show that the lateral displacement was perfectly symmetrical and increased progressively. Conversely, for structures with greater compactness (corresponding to a fixed $C_1 = 1.2$ and decreasing $C_2$ values), a lateral contraction was observed in the post-peak regime. A possion's ratio is calculated as the ratio between the lateral displacement and the axial (vertical) displacement, extracted from the nodal displacements in the simulation. In the case of $C_2 = 0.8$, a negative Poisson's ratio of up to −0.12 was observed.

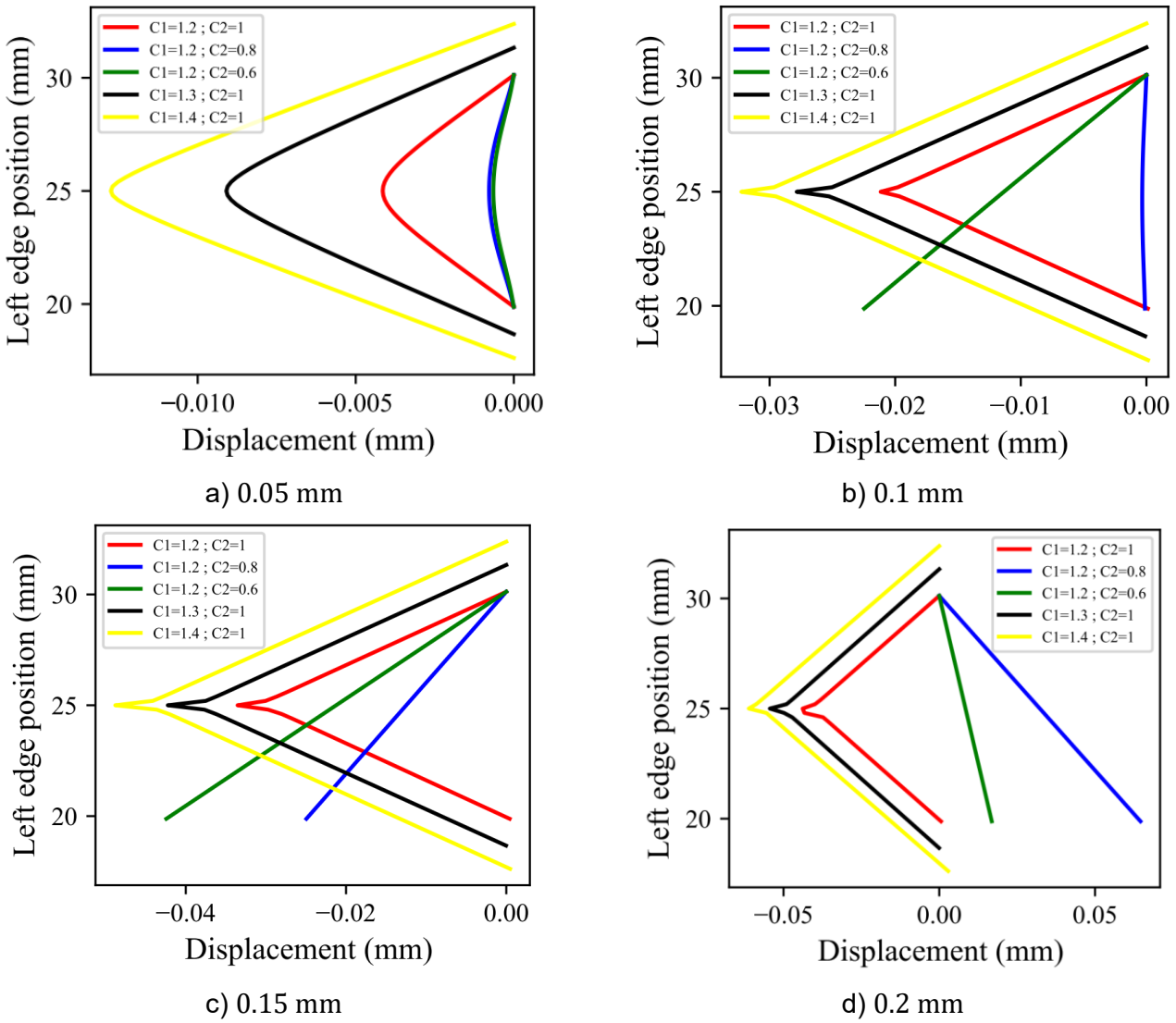


a) 0.05 mm b) 0.1 mm

c) 0.15 mm d) 0.2 mm

**Fig. 11.** Boundary displacement of the specimen under compression

Although this serves as a preliminary illustrative example, it demonstrates that this type of structure, when applied to a suitable problem, can play a significant role in enhancing the load-bearing capacity of a system.

This preliminary finding is highly significant, as it demonstrates that unique mechanical properties not present in the base material can be engineered merely by altering the geometric architecture. The practical implications of this are

substantial; the enhanced load-bearing capacity, for instance, stems from the material's tendency to draw mass inward toward a point of compression, thereby increasing its local density and stiffness. This unique behavior opens up a range of potential applications, from impact-resistant sandwich panel cores in aerospace and automotive structures, to biomedical devices such as expandable vascular stents and load-bearing implants, and personal protective equipment like body armor and helmets. To fully realize this potential, however, several avenues for future research must be pursued. Immediate next steps should include the experimental validation of these simulation results through the fabrication and mechanical testing of physical prototypes. Subsequently, a broader parametric study is warranted to optimize the geometric configuration for a maximum negative Poisson's ratio, followed by dynamic analysis under high-velocity impact loads to fully assess the structure's energy absorption capabilities for advanced protective applications.

## 5. Conclusion

A comprehensive numerical assessment of the elastic response and failure behavior of 2D Primitive TPMS lattice structures was conducted, considering variations in the geometric parameters $C_1$ and $C_2$. By employing a double phase-field damage model, we successfully captured the mechanical response from the initial elastic stage through to complete failure. The primary conclusions are as follows:

The mechanical performance of the structures is governed by both density and geometric shape. The importance of geometry was highlighted by a case where two structures of nearly identical density ($C_1 = 1.2,\ C_2 = 0.8$ and $C_1 = 1.4,\ C_2 = 1.0$) demonstrated a five-fold difference in strength.

The characteristic failure mechanism was found to originate at the specimen's center, which acts as the weakest point due to stress concentration, before propagating to the outer edges.

The ability to generate an auxetic effect (negative Poisson's ratio) in 2D Primitive structures by tuning geometric parameters was successfully demonstrated. A negative Poisson's ratio of $-0.12$ was achieved, showcasing the potential to engineer materials with unique, counter-intuitive mechanical properties.

These results provide critical insights that form a basis for the optimized design of 2D TPMS structures for specific applications. Future work should focus on experimental validation, broader parametric optimization, and dynamic analysis to fully exploit the potential of these architected materials.

## Acknowledgments

This research is funded by University of Transport and Communications (UTC) under grant number T2025-CT-006TD.

## References

[1] A. Joseph, V. Mahesh, D. Harursampath. (2021). On the application of additive manufacturing methods for auxetic structures: a review. *Advances in Manufacturing*, 9, 342–368. doi: 10.1007/s40436-021-00357-y

[2] M.G. Gado, O. Al-Ketan, M. Aziz, R.A. Al-Rub, S. Ookawara. (2024). Triply Periodic Minimal Surface Structures: Design, Fabrication, 3D Printing Techniques, State-of-the-Art Studies, and Prospective Thermal Applications for Efficient Energy Utilization. *Energy Technology*, 12(5), 2301287. doi: 10.1002/ente.202301287

[3] B.-A. Le, B.-V. Tran, T.-S. Vu, Q.-B. Nguyen, H.-Q. Nguyen, X. Chateau. (2024). Anisotropy and Mechanical Characteristics of Ultra-High Performance Concrete and Its Interpenetrating Phase Composite with Triply Periodic Minimal Surface Architectures. *Journal of Applied Mechanics*, 91(9), 091008. doi: 10.1115/1.4065901

[4] A. Jones, M. Leary, S. Bateman, M. Easton. (2022). Parametric design and evaluation of

TPMS-like cellular solids. *Materials & Design,* 221, 110908. doi: 10.1016/j.matdes.2022.110908

[5] Y. Xu, H. Zhang, E. Schlangen, M. Luković, B. Šavija. (2020). Cementitious cellular composites with auxetic behavior. *Cement and Concrete Composites*, 111, 103624. doi: 10.1016/j.cemconcomp.2020.103624

[6] M. Cervera, G.B. Barbat, M. Chiumenti, J.-Y. Wu. (2022). A Comparative Review of XFEM, Mixed FEM and Phase-Field Models for Quasi-brittle Cracking. *Archives of Computational Methods in Engineering*, 29, 1009-1083. https://doi.org/10.1007/s11831-021-09604-8

[7] H.-Q. Nguyen, B.-A. Le, B.-V. Tran, T.-S. Vu, T.-L. Bui. (2024). Deep artificial neural network-powered phase field model for predicting damage characteristic in brittle composite under varying configurations. *Machine Learning: Science and Technology*, 5(2), 025062. doi: 10.1088/2632-2153/ad52e8

[8] H.-Q. Nguyen, B.-V. Tran, T.-S. Vu. (2022). Numerical approach to predict the flexural damage behavior of pervious concrete. *Case Studies in Construction Materials*, 16, e00946. doi: 10.1016/j.cscm.2022.e00946

[9] H.Q. Nguyen, B.V. Tran, B.A. Le, T.T. Nguyen. (2024). On the choice of a phase field model for describing fracture behavior of concrete. *International Journal of Computational Materials Science and Engineering*, 13(1), 2350016. doi: 10.1142/S2047684123500161

[10] C. Miehe, F. Welschinger, M. Hofacker. (2010). Thermodynamically consistent phase-field models of fracture: Variational principles and multi-field FE implementations. *International Journal for Numerical Methods in Engineering*, 83(10), 1273–1311. doi: 10.1002/nme.2861

[11] P. Lenarda, J. Reinoso, M. Paggi. (2022). Multi-phase field approach to tensile fracture and compressive crushing in grained heterogeneous materials. *Theoretical and Applied Fracture Mechanics*, 122, 103632. doi: 10.1016/j.tafmec.2022.103632

[12] B. Bourdin, G.A. Francfort, J.-J. Marigo. (2000). Numerical experiments in revisited brittle fracture. *Journal of the Mechanics and Physics of Solids*, 48(4), 797–826. doi: 10.1016/S0022-5096(99)00028-9

[13] B. Bourdin, G.A. Francfort, J.-J. Marigo. (2008). The Variational Approach to Fracture. *Journal of Elasticity*, 91, 5-148. doi: 10.1007/s10659-007-9107-3

[14] C. Miehe, M. Hofacker, F. Welschinger. (2010). A phase field model for rate-independent crack propagation: Robust algorithmic implementation based on operator splits. *Computer Methods in Applied Mechanics and Engineering*, 199(45-48), 2765–2778. doi: 10.1016/j.cma.2010.04.011

[15] H.Q. Nguyen, B.V. Tran, B.A. Le, T.T. Nguyen. (2024). On the choice of a phase field model for describing fracture behavior of concrete. *International Journal of Computational Materials Science and Engineering*, 13(1), 2350016. doi: 10.1142/S2047684123500161

[16] H.-Q. Nguyen, G.-K. Le, T.Q. Bui, T.-L. Bui, B.-V. Tran. (2026). A micromechanics-based computational framework for predicting the elastic modulus and compressive strength of normal and high-performance concrete. *Computers & Structures*, 321, 108055. doi: 10.1016/j.compstruc.2025.108055